Journal of Materials Chemistry B

ROYAL SOCIETY OF CHEMISTRY

PAPER

View Article Online
View Journal | View Issue

Cite this: *J. Mater. Chem. B*, 2023, **11**, 5586

Choline phosphate lipid-hitchhiked near-infrared BODIPY nanoparticles for enhanced phototheranostics†

Huafeng Geng,[a] Wenhai Lin,[d] Junbao Liu,*[a] Qing Pei*[b] and Zhigang Xie*[bc]

Received 29th January 2023,
Accepted 21st April 2023

DOI: 10.1039/d3tb00175j

rsc.li/materials-b

Phototheranostics integrating optical imaging and phototherapy has attracted extensive attention. Achieving nanophototherapeutics with near infrared (NIR)-light synchronously triggered photodynamic therapy (PDT) and photothermal therapy (PTT) is challenging. Herein, we develop a multifunctional theranostic nanoplatform prepared from the co-assembly of NIR boron dipyrromethene (BODIPY) with a cooperative D–π–A structure of a thiophene-BODIPY core and benzene-diethylamino, and a choline phosphate lipid. The as-fabricated nanoparticles (DBNPs) exhibited desirable NIR absorption, uniform spherical morphology and good colloidal stability. The elaborate molecular design and supramolecular assembly endowed DBNPs with desirable PDT and PTT activities. Upon 808 nm laser irradiation, the DBNPs efficiently generated active singlet oxygen and regional hyperpyrexia, with a photothermal conversion efficiency of 37.6%. The excellent PDT and PTT performance of DBNPs boosted the potent *in vitro* and *in vivo* anti-tumor effects. In addition, these nanoparticles manifested their good capability of NIR fluorescence imaging of tumors. Overall, the DBNPs provide a paradigm for delivering hydrophobic phototherapy molecules with phospholipids for enhanced tumor treatment and imaging.

10th Anniversary Statement

We would like to extend our sincerest congratulations and deepest gratitude to you during the moment of the 10th anniversary of JMCB. JMCB reports hot spot research enabling spark academic front attention in the area of drug delivery, biomaterials and disease treatments. Detailed, JMCB exhibits its specialty on the materials synthesis, preparation, and biomedical application, and brings out significant ideology to boost further investigation in the field. It has become one of the most widely recognized and noted journals with the devotion of professional editorial team. We are fortunate to publish more than thirty works on versatile nanoformulations for antimicrobial and antitumor treatment with the support and help of editors and reviewers. We next would like to submit more research work to JMCB and hope to be recognized by JMCB. We believe that JMCB will lead the trend of material chemistry in the biomedical field and inspire emission and vitality to promote their booming development.

Introduction

Photothermal therapy (PTT) and photodynamic therapy (PDT) have shown great promise in tumor treatment as emerging light-triggered cancer therapies due to their remote controllability, low toxicity and non-invasiveness.[1–6] PDT uses photosensitizers to convert light energy to oxygen molecules and produces highly active singlet oxygen ($^1O_2$), thus causing irreversible apoptosis of tumor cells.[7–9] By contrast, PTT has the capability of transforming light energy into thermal energy *via* a non-radiative relaxation pathway, ultimately inducing devastating damage to cancer cells.[10–12] However, a single PDT or PTT modality has shown limited therapeutic effects *in vivo*.

[a] *Department of Obstetrics and Gynecology, China-Japan Union Hospital of Jilin University, No. 126, Xiantai Street, Changchun 130033, P. R. China. E-mail: junbao@jlu.edu.cn*
[b] *State Key Laboratory of Polymer Physics and Chemistry, Changchun Institute of Applied Chemistry, Chinese Academy of Sciences, Changchun, Jilin 130022, P. R. China. E-mail: peiqing@ciac.ac.cn, xiez@ciac.ac.cn*
[c] *School of Applied Chemistry and Engineering, University of Science and Technology of China, Hefei, Anhui 230026, P. R. China*
[d] *Biomedical Polymers Laboratory, College of Chemistry, Chemical Engineering and Materials Science, and State Key Laboratory of Radiation Medicine and Protection, Soochow University, Suzhou 215123, P. R. China*

† Electronic supplementary information (ESI) available: Materials, characterization, details on experimental procedures, and supplementary data Fig. See DOI: https://doi.org/10.1039/d3tb00175j

PDT has the intrinsic drawback of highly depending on an oxygen-rich environment.[13–15] PTT tends to cause uneven heat distribution within tumor tissues and induce heat shock response defense mechanisms to inhibit apoptosis, which results in the recurrence and metastasis of residual tumor tissues.[16,17] Combining PDT with PTT modalities is considered an excellent strategy to improve antitumor efficiency.[18–23] The PTT effect can increase oxygen perfusion into the tumor by accelerating intratumoral blood flow, which in turn relieves the tumor hypoxic microenvironment and amplifies the efficacy of PDT.[24,25] Besides, PDT-generated ROS may weaken the heat shock defense, thereby enhancing the PTT outcome.[26,27] However, most systems of combined PDT and PTT are realized by dual excitation wavelengths, which complicates the treatment process.[28–30] Besides, deep tissues are unreachable owing to the short wavelength limitation. For the phototherapy of deep malignant tissues, near-infrared (NIR) light is preferable due to its high penetration depth and minimal autofluorescence of biological species compared with UV/visible light.[31,32] Therefore, it is important to develop a single NIR laser irradiation-activated nanoplatform for combined PDT and PTT.

Boron dipyrromethene (BODIPY) dyes are widely used in phototherapy because of their low toxicity, high extinction coefficient, good photostability and facile chemical structures with an adjustable absorption spectrum.[7,33–36] The above-mentioned advantages contribute to their excellent PTT and PDT performance. However, the absorption wavelength of most BODIPY dyes cannot reach the NIR region, which limits their application in tumor treatment. Moreover, most BODIPY dyes are hydrophobic and possess poor pharmacokinetics and their availability is low.[34,37] Leveraging the nanoplatforms to deliver BODIPY can address these issues. Considering the strong hydrophobicity, phospholipids may be a good choice to obtain optimal nanoparticles with the aid of amphiphilic structures. Besides, zwitterionic structures are favorable for avoiding the non-specific absorption of serum albumin during the *in vivo* process. Among the phospholipids, the choline phosphate lipid with reversed zwitterions in comparison with the traditional phosphatidylcholine lipid is preferred in drug delivery owing to the modifiability, enhanced endocytosis efficiency, better resistance to protein adsorption, and stronger hydrophilicity.[38–40]

Herein, we synthesized a NIR BODIPY molecule and used the choline phosphate lipid (DPCP) as the carrier to form stable nanoparticles (DBNPs) in aqueous solutions *via* the nanoprecipitation method (Scheme 1). The assembled behavior and colloidal stability of the as-prepared nanoparticles were evaluated. We examined the photo-physical properties of DBNPs and confirmed the successful co-assembly. The PTT and PDT performance was systematically investigated. Due to the supramolecular interaction of DPCP with the phospholipid of the cell membranes, the DBNPs were internalized by tumor cells and exhibited potent photo-induced cytotoxicity.[40] Promising phototheranostics with NIR fluorescence imaging-instructed PDT/PTT was achieved upon single NIR irradiation (808 nm).

Results and discussion

Synthesis of NIR-BODIPY and DPCP

Most BODIPY dyes are hydrophobic and their absorption wavelength cannot reach the near-infrared region.[41,42] We first designed and synthesized a NIR BODIPY molecule (compound **2**) (Fig. S1, ESI†). The designed NIR-BODIPY has a D–π–A structure through the construction of the thiophene-BODIPY core and benzene-diethylamino cooperation, and high-efficiency intramolecular charge transfer (ICT) from a thiophene moiety to a diethylamino moiety is expected to ensure an enhanced and red shifted absorption.[43] Besides, the diethylamino group can induce ICT to decrease the fluorescence of BODIPY. The weakening of radiative transition could lead to more energy release by non-radiative transition pathways. Thus, BODIPY has the good potential to enhance the PTT effect. In detail, 2-thenaldehyde and 2-methyl-1*H*-pyrrole were stirred in the presence of trifluoroacetic acid (TFA), and 2,3-dichloro-5,6-dicyano-1,4-benzoquinone was added and stirred for an additional 2 h. Then, Et_3N and $BF_3 \cdot Et_2O$ were added under ice-cold conditions and stirred for another 8 h. Compound **1** shown in Fig. S1 (ESI†) was obtained after the extraction and purification through silica gel column chromatography. The mixture of compound **1**, 4-(diethylamino) benzaldehyde, piperidine and acetic acid were refluxed (120 °C) for 3 h to produce NIR-BODIPY. The chemical structures of NIR-BODIPY were validated by proton nuclear magnetic resonance (^{1}H NMR) spectroscopy and electrospray ionization mass spectrometry (ESI-MS) (Fig. S2 and S3, ESI†). The synthesis of DPCP follows the previously reported method.[38,39]

Preparation and characterization of DBNPs

In order to solve the hydrophobic issues of BODIPY, we co-assembled BODIPY with a phospholipid to increase the stability and prolong the blood circulation time. The nanoprecipitation method was used to prepare nanosuspensions (DBNPs) by the co-assembly of BODIPY and DPCP. In detail, tetrahydrofuran (THF) solutions of BODIPY and DPCP were dropwise added to deionized water with vigorous stirring. The DBNPs were obtained after completely removing the organic solvent. The BODIPY loading capability was calculated to be 7.3 wt%. The synthesized DBNPs had an average hydrodynamic diameter of 178.5 nm and an average polydispersity index (PDI) of 0.184, as determined by dynamic light scattering (DLS) (Fig. 1a), indicating the homogeneous distribution of nanoparticles. The ζ-potential of DBNPs was −28.67 mV. Meanwhile, the BODIPY alone could form big aggregates with a particle size of approximately 900 nm (Fig. S4, ESI†), which is not suitable for *in vivo* delivery. Such results confirmed that DPCP played a vital role in improving BODIPY assembly. The spherical morphology of DBNPs was confirmed by transmission electron microscopy (TEM) images (Fig. 1b). Next, we studied the optical properties of DBNPs. BODIPY had a NIR absorption and the maximum absorption peak reached 751 nm. The absorption spectrum of DBNPs broadened and red-shifted by about 33 nm, compared with that of BODIPY molecules (Fig. 1c), indicating the formation of J-aggregation of BODIPY molecules due to their π–π stacking.

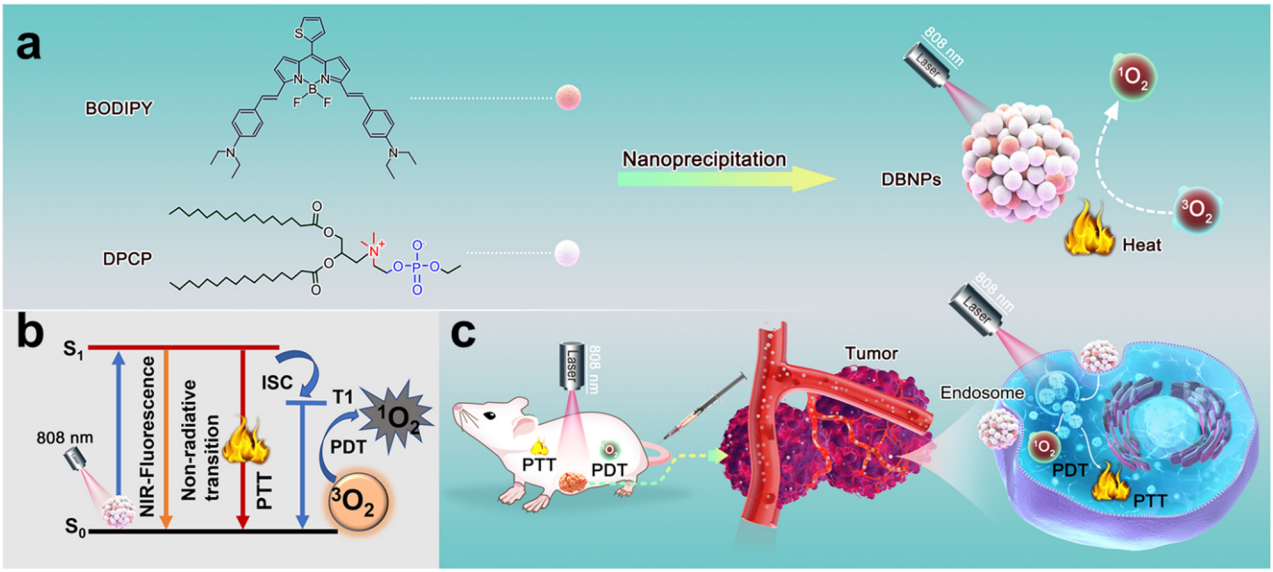

Scheme 1 A schematic of the DBNP preparation (a), the generated mechanism of fluorescence, PTT and PDT upon NIR laser irradiation (b), and the antitumor application of DBNPs integrating PDT and PTT (c).

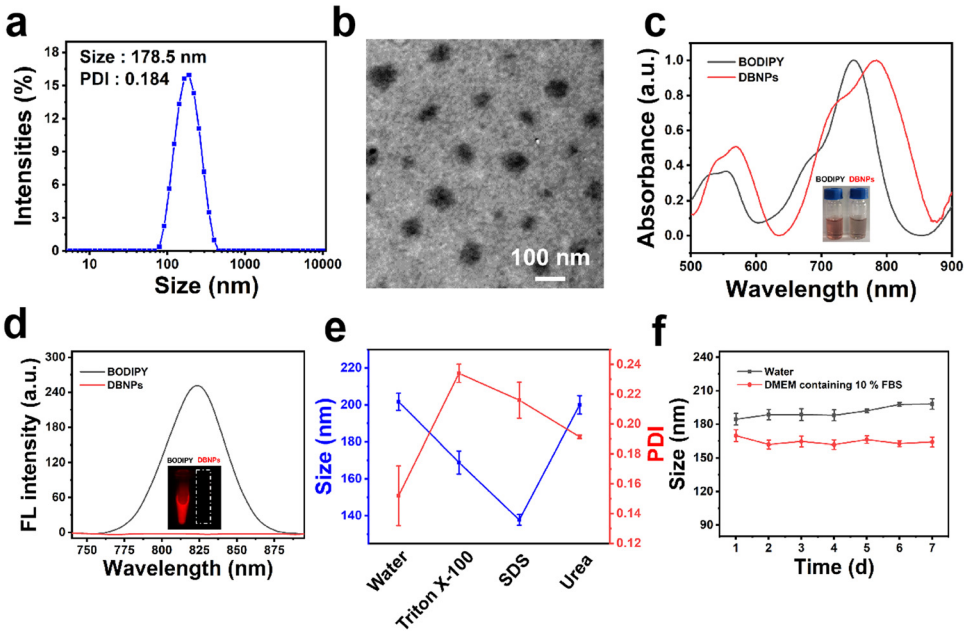

Fig. 1 Characterization of DBNPs. The (a) size distribution and (b) TEM image of DBNPs. Scale bar, 100 nm. (c) Normalized absorption spectra of BODIPY in THF and DBNPs in water with corresponding photographs (inset). (d) Fluorescence spectra and photographs of BODIPY in THF and DBNPs at an equivalent BODIPY concentration of 12.5 μg mL^{-1} in water. (e) The study of an assembly driving force by incubating DBNPs with water and three other different media, including Triton X-100, water, sodium dodecyl sulfate (SDS) and urea. (f) Stability of DBNPs in water and DMEM containing 10% FBS for 7 days as determined by DLS.

The dark salmon color of BODIPY in THF changed to gray-brown of DBNPs in water. Compared with free BODIPY in THF, DBNPs exhibited obvious quenched fluorescence, further demonstrating the π–π stacking of BODIPY molecules (Fig. 1d). The fluorescence quantum yield of DBNPs was calculated to be 0.1%. The quenching radiation energy is in favor of the enhanced photothermal performance of DBNPs.[44] We next investigated the assembly mechanism of the two molecules. As shown in Fig. 1e, Triton X-100 treatment resulted in a significantly decreased particle size and increased PDI, confirming the dominant role of hydrophobic interactions in the assembly process. DBNPs were stored at 4 °C in water and the Dulbecco's modified Eagle's medium (DMEM) containing 10% fetal bovine serum (FBS) for one week, and the size and PDI were monitored for 7 day. As shown in Fig. 1f, a

negligible change was observed during the testing process. At the same time, there was no macroscopical aggregation and precipitation in the nanosuspensions (Fig. S5, ESI†). The results validated the excellent colloidal stability of DBNPs.

Photothermal performance of DBNPs

The strong NIR absorption of DBNPs encouraged us to explore the photothermal effects at different concentrations and laser power densities. The DBNPs were exposed to an 808 nm laser with a power of 0.8 W cm^{-2} for 5 min, and the temperature was recorded at specific times using a thermocouple. DBNPs exhibited different degrees of temperature increase as the BODIPY concentrations of DBNPs ranged from 0 to 50 μg mL^{-1} (Fig. 2a). Excitingly, the temperature of DBNPs at a BODIPY concentration of only 12.5 μg mL^{-1} could reach 44.4 °C within 2 min, with the highest temperature achieved as high as 54.7 °C, which was far above the threshold (42 °C) to cause severe thermotherapeutic damage to cancer cells.[45] Similarly, for DBNPs with a constant BODIPY concentration (12.5 μg mL^{-1}), higher power densities of laser irradiation led to higher temperatures (Fig. 2b). Infrared thermal imaging was performed and the results verified the increase in the temperature of DBNPs under laser irradiation (Fig. 2c). Through repeated irradiation/cooling cycles, we evaluated the photothermal stability of the DBNPs. As can be seen in Fig. 2d, the maximum temperature increase of DBNPs remained almost unchanged after four on/off cycles of laser, indicating their excellent photothermal stability. Photothermal conversion efficiency, as an important index of photothermal agents, was also investigated. Aqueous solutions of DBNPs were subjected to 808 nm laser irradiation (0.8 W cm^{-2}). The temperature peaked at 5 min, after which the laser was turned off (Fig. 2e). The photothermal conversion efficiency was calculated to be 37.6% by plotting the linear time data from the DBNP temperature drop period against the negative natural logarithm of the change in temperature as reported in the study by Roper *et al.* (Fig. S6, ESI†).[46] In addition, the photostability of DBNPs was compared with that of indocyanine green (ICG), a drug approved by the Food and Drug Administration (FDA). The absorbance of ICG was significantly reduced after 5 min laser irradiation (808 nm, 0.8 W cm^{-2}), accompanied by a color change from bright green to yellow. By contrast, the absorption spectra and color of DBNPs negligibly changed (Fig. 2f and Fig. S7, ESI†). The photothermal performance and photostability of NIR-BODIPY in dimethyl formamide (DMF) were also investigated (Fig. S8a and b, ESI†). DBNPs exhibited better photostability compared with free BODIPY in DMF. In summary, the high photothermal conversion efficiency and excellent photothermal stability suggest DBNPs' great potential in tumor PTT.

The $^1O_2$ production capacity of DBNPs

We performed theoretical studies on NIR-BODIPY to explore the intersystem crossing efficiency.[47] There is an energy gap (ΔE_{ST} = 0.91 eV) between the lowest singlet excited state (S1) and the lowest triplet excited state (T1) (Fig. S9, ESI†). Thus, the S1-to-T1 ISC process of heavy-atom-free NIR-BODIPY can proceed,[48] which facilitates the transition from $^3O_2$ to $^1O_2$. We then investigated the ability of DBNPs to generate $^1O_2$ by using 1,3-diphenylisobenzofuran (DPBF) as the $^1O_2$ scavenger. After 70 s of 808 nm laser irradiation, the absorption peak of DPBF at 422 nm was observed to decrease obviously in the presence of

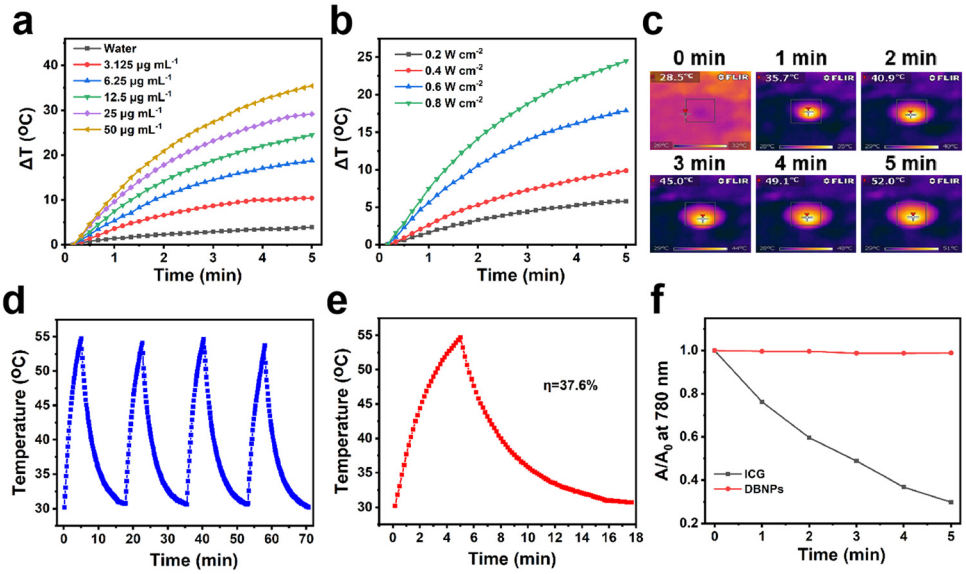

Fig. 2 DBNPs' photothermal performance and photostability. Photothermal properties of (a) various BODIPY concentrations (0–50 μg mL^{-1}) of DBNPs under laser irradiation (808 nm, 0.8 W cm^{-2}), and (b) DBNPs at a BODIPY concentration of 12.5 μg mL^{-1} under laser irradiation of different power densities (808 nm, 0.2–0.8 W cm^{-2}). (c) Infrared thermal images of DBNPs at a BODIPY concentration of 12.5 μg mL^{-1} under laser irradiation (808 nm, 0.8 W cm^{-2}) for 5 min. (d) Temperature change curves of DBNPs undergoing four cycles of irradiation/cooling. (e) Photothermal effect of DBNPs at a BODIPY concentration of 12.5 μg mL^{-1} under laser irradiation (808 nm, 0.8 W cm^{-2}) for 5 min, followed by laser removal. (f) Stability comparison by the absorbance decay rates of DBNPs and ICG under laser irradiation (880 nm, 0.8 W cm^{-2}) for 5 min.

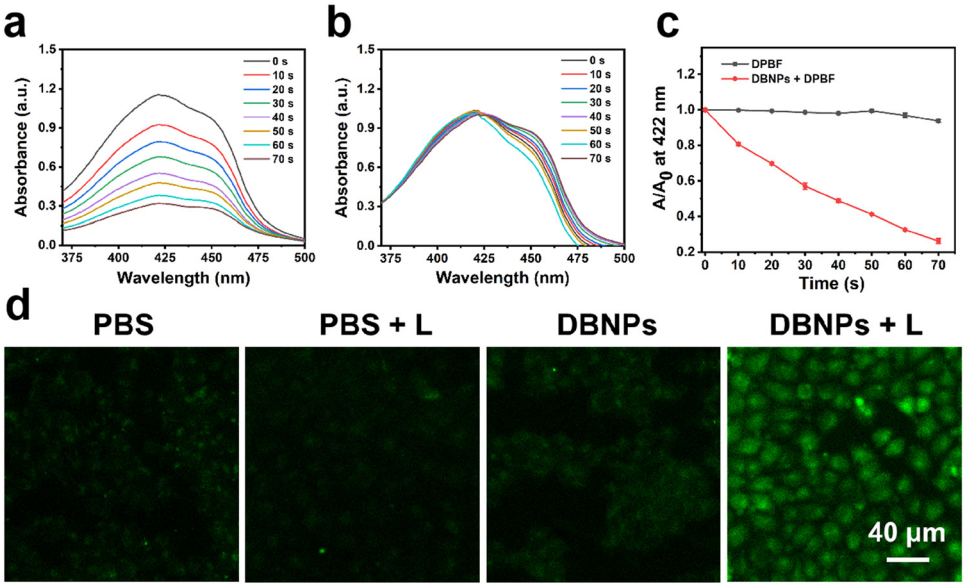

Fig. 3 The absorption spectra of DPBF in the presence (a) and absence (b) of DBNPs (BODIPY concentration: 0.75 μg mL^{-1}) under laser irradiation (808 nm, 0.8 W cm^{-2}) for 70 s. (c) The corresponding decay rates of DPBF at 422 nm with/without DBNPs (BODIPY concentration: 0.75 μg mL^{-1}) upon irradiation (808 nm laser, 0.8 W cm^{-2}) for 70 s. (d) Intracellular $^1O_2$ generation in HeLa cells mediated by DBNPs (BODIPY concentration: 20 μg mL^{-1}) under laser irradiation (808 nm, 0.2 W cm^{-2}) for 10 min using DCFH-DA as the indicator. Scale bar, 40 μm.

DBNPs (Fig. 3a), indicating that DBNPs have a robust $^1O_2$ generation capacity. In contrast, negligible spectra changes were observed in the control group (DPBF + L) (Fig. 3b). According to the DPBF degradation kinetic curves under laser irradiation with the present DBNPs, the resulting reduction in DPBF absorbance was 84% in 70 s (Fig. 3c). The good $^1O_2$ generation of NIR-BODIPY in DMF was also confirmed (Fig. S8c, ESI†). In addition, we investigated the intracellular ROS levels in response to various treatments using the indicator 2′,7′-dichlorofluorescein diacetate (DCFH-DA). Non-fluorescent DCFH-DA was able to easily pass through cell membranes and, upon entering the cell, was degraded by intracellular esterase to produce DCFH. The DCFH can be rapidly converted by intracellular reactive oxygen species to green fluorescent 2′,7′-dichlorofluorescein (DCF). As can be seen in Fig. 3d, DBNP-treated cells exhibited strong green fluorescence under 808 nm laser irradiation (0.2 W cm^{-2}, 10 min), whereas the control groups (PBS, PBS + L, and DBNPs) showed weak fluorescence under the same conditions. We obtained similar results on 4T1 cells (Fig. S10, ESI†). These results demonstrated that DBNPs could efficiently produce $^1O_2$.

Cell uptake and phototherapy effect of DBNPs

Using confocal laser scanning microscopy (CLSM), we first investigated the cellular uptake of DBNPs. CLSM images showed an increased red fluorescence intensity as the incubation time increased from 2 to 6 h, indicating the effective, time-dependent internalization of DBNPs by HeLa cells. The energy-required endocytosis was confirmed by the significant differential fluorescence in HeLa cells treated with DBNPs at 4 °C and 37 °C (Fig. S11a, ESI†). The similar results were confirmed for 4T1 cells (Fig. S11b, ESI†). The cytotoxicity of DBNPs against HeLa cells with/without (light/dark) laser irradiation was investigated using the 3-(4,5-dimethylthiazol-2-yl)-2,5-diphenyltetrazolium bromide (MTT) assay. DBNPs had ignorable cytotoxicity towards HeLa cells even at a high BODIPY concentration of 15 μg mL^{-1} in the absence of light irradiation (Fig. 4a). Under laser irradiation (808 nm, 0.8 W cm^{-2}) for 5 min, the cell viability decreased

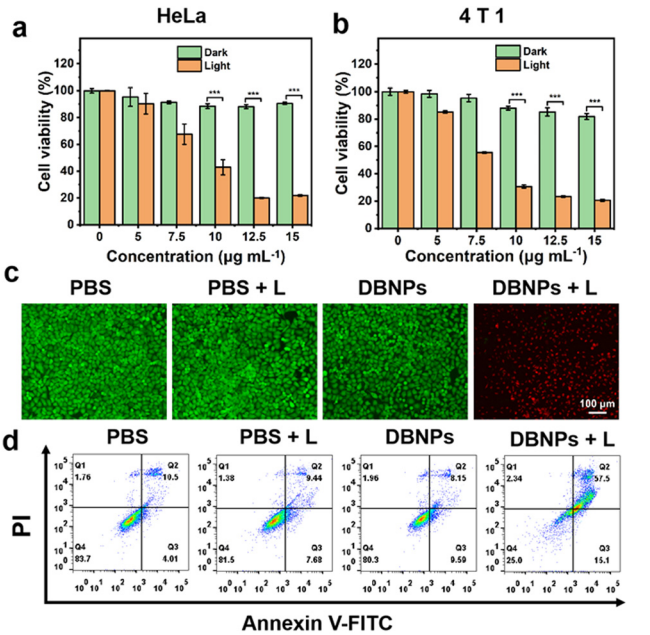

Fig. 4 The *in vitro* phototherapy effect of DBNPs. The cell viability of DBNPs toward HeLa (a) and 4T1 (b) cells without or with laser irradiation (808 nm, 0.8 W cm^{-2}, 5 min). (c) Live/dead staining images and (d) cell apoptosis analysis of HeLa cells incubated with DBNPs (BODIPY concentration: 12.5 μg mL^{-1}) without or with laser irradiation (808 nm, 0.8 W cm^{-2}) for 5 min. Scale bar, 100 μm. Statistical *P*-values: ***$P < 0.001$.

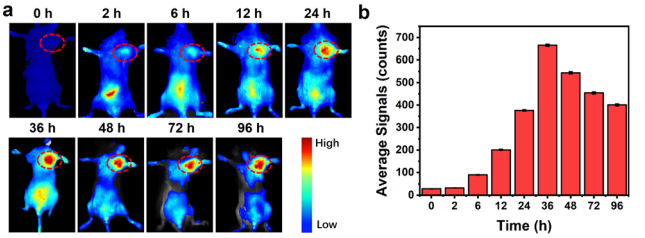

Fig. 5 *In vivo* NIR fluorescence imaging of DBNPs. (a) NIR fluorescence images, and (b) the corresponding intratumoral fluorescence signals of the mouse intravenously treated with DBNPs (BODIPY dose: 3.5 mg kg^{-1}). Tumor regions are marked with dotted red cycles.

gradually with increasing concentrations (5–15 μg mL^{-1}), with a cell survival rate of only 21.9% at a 15 μg mL^{-1} BODIPY concentration. The phototoxicity of DBNPs was also potent for 4T1 cells (Fig. 4b). In order to investigate the contribution of PDT and PTT to antitumor activity, we supplemented the cytotoxicity of the single PDT (NPs + 4 °C + L) and PTT (NPs + 37 °C + Vc + L) groups. As shown in Fig. S12 (ESI†), the obviously decreased viability of DBNPs with the treatment of 4 °C or vitamin C (Vc) confirmed that both PDT and PTT participated in the antitumor effect. More potent cytotoxicity of the Vc-treated group compared with the 4 °C-treated group implied the predominant role of the PTT effect on cellular death. Live/dead cell staining experiments were performed on HeLa cells to visualize the photoactivity of DBNPs by distinguishing dead cells from live cells. Propidium iodide (PI) can stain dead cells red, whereas calcein-acetoxymethyl (Calcein-AM) stains living cells green. As shown in Fig. 4c, only DBNP-treated cells with laser irradiation showed red fluorescence, while the control groups (PBS, PBS + L, and DBNPs) exhibited the full vision of green fluorescence. The results confirmed the cytotoxicity of DBNPs mediated by the PTT and PDT effects upon laser irradiation. The superior photo-toxicity toward 4T1 cells was also evaluated through Calcein-AM and PI staining assays (Fig. S13, ESI†). Besides, the annexin-V FITC/PI double staining method was used to quantify apoptosis and necrosis. As shown in Fig. 4d, cells in the DBNPs + L group had a late apoptotic rate of up to 57.5%, implying that the main cell death was mediated through the apoptosis pathway.

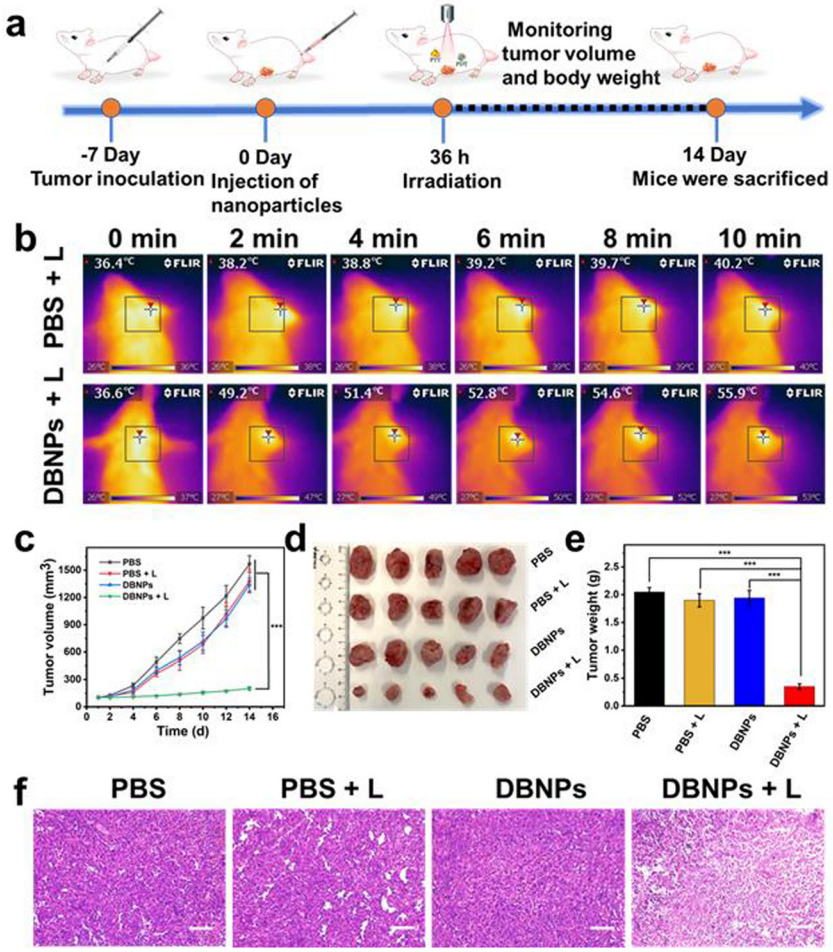

Fig. 6 (a) A schematic diagram of animal treatment. (b) Infrared thermal images of mice treated with DBNPs at a BODIPY dose of 3.5 mg kg^{-1} and PBS under laser irradiation for 10 min (808 nm, 0.8 W cm^{-2}). (c) The tumor volume growth curves of 4T1 tumor-bearing mice with different treatments (n = 5). (d) The pictures and (e) weight of the dissected tumors in different groups (PBS, PBS + L, DBNPs and DBNPs + L). (f) H&E-staining images of tumor tissues in four different groups (PBS, PBS + L, DBNPs, and DBNPs + L). Scale bars, 100 μm. Statistical P-values: ***$P < 0.001$.

In vivo NIR fluorescence imaging of DBNPs

Female BALB/c mice were used to explore the *in vivo* imaging ability of DBNPs. Mice were treated with intravenous injections of DBNPs, and fluorescence images of the mice were taken at specified times. As can be seen in Fig. 5a and b, the fluorescence signal of the tumor gradually grew as time went by and peaked at 36 h. The fluorescence imaging guides the optimal treatment regimen.

Therefore, the appropriate time for irradiation treatment should be 36 h after the tail vein injection. In comparison, noticeable fluorescence was observed in spleen and liver tissues at 2 h and 6 h after injection, respectively. Even after 96 h post-administration, bright fluorescence was still visible in the tumors, which contributed to repeated phototherapy by laser irradiation without the additional injection of formulations. Meanwhile, significantly decreased fluorescence was seen in other tissues. The fluorescence images of excised major organs confirmed the *in vivo* metabolic processes through liver and spleen (Fig. S14, ESI†). The tiny size and strong photostability of DBNPs were credited for the quick and reliable imaging of malignancies. These findings suggested that DBNPs would be a promising tumor therapeutic candidate.

In vivo phototherapy effect of DBNPs

To further evaluate the PTT and PDT performance of DBNPs *in vivo*, we have constructed a subcutaneous 4T1 tumor xenograft model (Fig. 6a). Mice were divided into four groups, *i.e.*, PBS, PBS + L, DBNPs and DBNPs + L, at random when the tumor volume reached 80–100 mm^3. DBNPs were administered intravenously to mice at a dose of 3.5 mg kg^{-1} BODIPY. Thirty-six hours after injection, the tumor sites of the mice in the PBS + L and DBNPs + L groups were exposed to an 808 nm laser for 10 min at a power intensity of 0.8 W cm^{-2}. Every two minutes during irradiation, infrared thermal pictures were taken to track the intratumoral temperature (Fig. 6b). The tumors that were given DBNP treatment reached a maximal temperature of 55.9 °C, whereas tumor temperatures in mice given PBS only increased to 40.2 °C. These findings revealed that DBNPs might accumulate at tumor tissues efficiently and provide sizable photothermal effects, which is necessary for efficient phototherapy *in vivo*. In PBS, PBS + L and DBNPs groups, tumor volumes of mice gradually increased from an initial volume of approximately 100 mm^3 to 1200–1600 mm^3 within 2 weeks, suggesting that neither laser irradiation nor DBNPs could inhibit tumor growth (Fig. 6c). At day 14, tumors were collected from sacrificed mice and photographed (Fig. 6d). The smallest tumors in the DBNPs + L group revealed the excellent tumor suppression efficiency of DBNPs through the combination of PTT and PDT under irradiation. The tumor weights agreed well with the tumor volume growth trends (Fig. 6e). To examine the anticancer efficacy of DBNPs, tumor slices received H&E staining (Fig. 6f). The results demonstrated that the low-temperature increase caused by the single laser irradiation had no damaging impact on the tumor tissue. Meanwhile, extensive tumor nuclear ablation was observed in the DBNPs + L group.

Finally, we studied the biosafety of DBNPs. Hemocompatibility was confirmed by negligible hemolytic activity (Fig. S15, ESI†). As shown in Fig. S16a (ESI†), the mice's body weight increased gradually in each of the four groups, indicating the DBNPs' strong biocompatibility. We also checked relevant blood indicators, and no obvious abnormalities were seen in the DBNPs + L group (Fig. S16b, ESI†). The results of H&E staining of major organs showed that DBNPs did not cause significant tissue damage (Fig. S16c, ESI†).

Conclusions

In summary, we achieved engineered phototheranostics based on hydrophobic BODIPY-hitchhiked phospholipids for cancer imaging and combined PDT/PTT. The thiophene-BODIPY core and benzene-diethylamino cooperation and supramolecular assembly endowed the BODIPY with NIR absorption and superior PDT and PTT performance. The assembly of DPCP and BODIPY was driven by hydrophobic interactions. The as-prepared DBNPs exhibited good colloidal stability. DBNPs had excellent photoactivity as shown by the efficient $^1O_2$ generation and photothermal conversion capacity (η = 37.6%) upon NIR light irradiation. The DBNPs exhibited potent cytotoxicity by virtue of the combination of PTT and PDT. Furthermore, DBNPs could rapidly accumulate at tumor sites and exhibit significant temperature elevation and efficient inhibition of tumor growth *in vivo* after an intravenous injection. We believe that the integration of phototherapy agents and phospholipids into one formulation could be a promising strategy and have great clinical translation potential for achieving imaging-guided cancer treatment.

Author contributions

Huafeng Geng: investigation, validation, data curation, and writing – original draft. Wenhai Lin: investigation and formal analysis. Junbao Liu: funding acquisition, writing – review and editing, and supervision. Qing Pei: conceptualization, formal analysis, methodology, funding acquisition, writing – review and editing, and supervision. Zhigang Xie: conceptualization, resources, writing – review and editing, funding acquisition, supervision, and project administration.

Conflicts of interest

There are no conflicts to declare.

Acknowledgements

We greatly acknowledge the financial support from the National Natural Science Foundation of China (Project No. 52203199 and 51973214) and the Natural Science Foundation of Jilin Province (Project No. YDZJ202101ZYTS013). We thank professor Xifei Yu for providing the material of DPCP.

Notes and references

1 Y. Song, Y. Li, Y. Zhang, L. Wang and Z. Xie, *J. Mater. Chem. B*, 2019, **7**, 7776–7782.
2 N. Song, L. Fu, Y. Liu, Y. Li, L. Chen, X. Wang, S. Liu and Z. Xie, *Dyes Pigm.*, 2019, **162**, 295–302.
3 M. R. Younis, C. Wang, R. An, S. Wang, M. A. Younis, Z. Q. Li, Y. Wang, A. Ihsan, D. Ye and X. H. Xia, *ACS Nano*, 2019, **13**, 2544–2557.
4 Q. Wang, Y. Dai, J. Xu, J. Cai, X. Niu, L. Zhang, R. Chen, Q. Shen, W. Huang and Q. Fan, *Adv. Funct. Mater.*, 2019, **29**, 1901480.
5 T. Jin, D. Cheng, G. Jiang, W. Xing, P. Liu, B. Wang, W. Zhu, H. Sun, Z. Sun, Y. Xu and X. Qian, *Bioact. Mater.*, 2022, **14**, 42–51.
6 P. Zhang, Q. Wu, J. Yang, M. Hou, B. Zheng, J. Xu, Y. Chai, L. Xiong and C. Zhang, *Acta Biomater.*, 2022, **146**, 450–464.
7 W. Sun, X. Zhao, J. Fan, J. Du and X. Peng, *Small*, 2019, **15**, 1970167.
8 M. Lan, S. Zhao, W. Liu, C.-S. Lee, W. Zhang and P. Wang, *Adv. Healthcare Mater.*, 2019, **8**, 1900132.
9 S. Li, F. Yang, Y. Wang, T. Du and X. Hou, *Chem. Eng. J.*, 2023, **451**, 138621.
10 D. Zhi, T. Yang, J. O'Hagan, S. Zhang and R. F. Donnelly, *J. Controlled Release*, 2020, **325**, 52–71.
11 C. Li, Y. Cheng, D. Li, Q. An, W. Zhang, Y. Zhang and Y. Fu, *Int. J. Mol. Sci.*, 2022, **23**, 7909–7924.
12 H. Sun, Q. Zhang, J. Li, S. Peng, X. Wang and R. Cai, *Nano Today*, 2021, **37**, 101073.
13 J. F. Algorri, M. Ochoa, P. Roldán-Varona, L. Rodríguez-Cobo and J. M. López-Higuera, *Cancers*, 2021, **13**, 3484–3525.
14 X. Deng, Z. Shao and Y. Zhao, *Adv. Sci.*, 2021, **8**, 2002504.
15 J. Zhou, Q. Wang, S. Geng, R. Lou, Q. Yin and W. Ye, *Mater. Sci. Eng., C*, 2019, **102**, 541–551.
16 J. Chen, C. Ning, Z. Zhou, P. Yu, Y. Zhu, G. Tan and C. Mao, *Prog. Mater. Sci.*, 2019, **99**, 1–26.
17 J. Li, W. Zhang, W. Ji, J. Wang, N. Wang, W. Wu, Q. Wu, X. Hou, W. Hu and L. Li, *J. Mater. Chem. B*, 2021, **9**, 7909–7926.
18 Q. Wang, B. Xia, J. Xu, X. Niu, J. Cai, Q. Shen, W. Wang, W. Huang and Q. Fan, *Mater. Chem. Front.*, 2019, **3**, 650–655.
19 W. Wang, F. Wu, Q. Zhang, N. Zhou, M. Zhang, T. Zheng, Y. Li and B. Z. Tang, *ACS Nano*, 2022, **16**, 7961–7970.
20 W. Zeng, H. Zhang, Y. Deng, A. Jiang, X. Bao, M. Guo, Z. Li, M. Wu, X. Ji, X. Zeng and L. Mei, *Chem. Eng. J.*, 2020, **389**, 124494.
21 E. Pang, R. Huang, S. Zhao, K. Yang, B. Li, Q. Tan, S. Tan, M. Lan, B. Wang and X. Song, *J. Mater. Chem. B*, 2022, **10**, 9848–9854.
22 H. Zhu, X. Zhang, Q. Wang, J. Deng, Z. Zhang, X. Zhang, J. Cao and B. He, *J. Mater. Chem. B*, 2022, **10**, 10083–10096.
23 L. Fu, Y. Huang, J. Hou, M. Sun, L. Wang, X. Wang and L. Chen, *J. Mater. Chem. B*, 2022, **10**, 8432–8442.
24 X. Liu, N. Xu, X. Pu, J. Wang, X. Liao, Z. Huang and G. Yin, *J. Mater. Chem. B*, 2022, **10**, 4605–4614.
25 X. Liu, R. Li, Y. Zhou, W. Lv, S. Liu, Q. Zhao and W. Huang, *J. Colloid Interface Sci.*, 2022, **608**, 1543–1552.
26 Y. Zhong, X. Zhang, L. Yang, F. Liang, J. Zhang, Y. Jiang, X. Chen and F. Ren, *Mater. Sci. Eng., C*, 2021, **131**, 112524.
27 P. Xue, R. Yang, L. Sun, Q. Li, L. Zhang, Z. Xu and Y. Kang, *Nano-Micro Lett.*, 2018, **10**, 74.
28 S. S. Kelkar, E. McCabe-Lankford, R. Albright, P. Harrington and N. H. Levi-Polyachenko, *Lasers Surg. Med.*, 2016, **48**, 893–902.
29 S. M. Ardekani, A. Dehghani, M. Hassan, M. Kianinia, I. Aharonovich and V. G. Gomes, *Chem. Eng. J.*, 2017, **330**, 651–662.
30 X. Tan, X. Pang, M. Lei, M. Ma, F. Guo, J. Wang, M. Yu, F. Tan and N. Li, *Int. J. Pharm.*, 2016, **503**, 220–228.
31 G. Hong, A. L. Antaris and H. Dai, *Nat. Biomed. Eng.*, 2017, **1**, 0010.
32 X. Lian, M. Y. Wei and Q. Ma, *Front. Bioeng. Biotechnol.*, 2019, **7**, 386.
33 L. Huang and G. Han, *Small Methods*, 2018, **2**, 1700370.
34 T. Zhang, C. Ma, T. Sun and Z. Xie, *Coord. Chem. Rev.*, 2019, **390**, 76–85.
35 Y. Zhang, R. Zhao, J. Liu, H. Kong, K. Zhang, Y.-N. Zhang, X. Kong, Q. Zhang and Y. Zhao, *Biomaterials*, 2021, **275**, 120945.
36 H. Dang, D. Yin, Y. Tian, Q. Cheng, C. Teng, Y. Xu and L. Yan, *J. Mater. Chem. B*, 2022, **10**, 5279–5290.
37 Z. Mao, J. H. Kim, J. Lee, H. Xiong, F. Zhang and J. S. Kim, *Coord. Chem. Rev.*, 2023, **476**, 214908.
38 S. Li, W. Mei, X. Wang, S. Jiang, X. Yan, S. Liu and X. Yu, *Chem. Commun.*, 2021, **57**, 1372–1375.
39 S. Li, X. Xie, W. Wang, S. Jiang, W. Mei, Y. Zhang, S. Liu and X. Yu, *Nanoscale*, 2022, **14**, 2277–2286.
40 W. Wang, S. Jiang, S. Li, X. Yan, S. Liu, X. Mao and X. Yu, *Chem. Mater.*, 2021, **33**, 774–781.
41 C. S. Kue, S. Y. Ng, S. H. Voon, A. Kamkaew, L. Y. Chung, L. V. Kiew and H. B. Lee, *Photochem. Photobiol. Sci.*, 2018, **17**, 1691–1708.
42 W. Zhang, A. Ahmed, H. Cong, S. Wang, Y. Shen and B. Yu, *Dyes Pigm.*, 2021, **185**, 108937.
43 L. Zhang, J. M. Cole, P. G. Waddell, K. S. Low and X. Liu, *ACS Sustainable Chem. Eng.*, 2013, **1**, 1440–1452.
44 J. Yin, X. Jiang, G. Sui, Y. Du, E. Xing, R. Shi, C. Gu, X. Wen, Y. Feng, Z. Shan and S. Meng, *J. Mater. Chem. B*, 2021, **9**, 7461–7471.
45 Z. Wang, M. Wang, X. Wang, Z. Hao, S. Han, T. Wang and H. Zhang, *Biosens. Bioelectron.*, 2023, **220**, 114883.
46 W. Shao, C. Yang, F. Li, J. Wu, N. Wang, Q. Ding, J. Gao and D. Ling, *Nano-Micro Lett.*, 2020, **12**, 147.
47 Y.-F. Kang, W.-K. Chen, K.-X. Teng, L.-Y. Wang, X.-C. Xu, L.-Y. Niu, G. Cui and Q.-Z. Yang, *CCS Chem.*, 2022, **4**, 3516–3528.
48 C. Li, T. Sun, X. Li and Z. Xie, *ACS Appl. Nano Mater.*, 2022, **5**, 18691–18696.